









# De novo design of $\text{Au}_{36}(\text{SR})_{24}$ nanoclusters

Xu Liu <sup>1,6</sup>, Wen Wu Xu <sup>2,6</sup>, Xinyu Huang <sup>3,6</sup>, Endong Wang<sup>4</sup>, Xiao Cai<sup>1</sup>, Yue Zhao <sup>1</sup>, Jin Li<sup>5</sup>, Min Xiao <sup>3</sup>, Chunfeng Zhang <sup>3</sup>✉, Yi Gao <sup>4</sup>✉, Weiping Ding<sup>1</sup> & Yan Zhu <sup>1</sup>✉

The discovery of atomically precise nanoclusters is generally unpredictable, and the rational synthesis of nanoclusters guided by the theoretical design is still in its infancy. Here we present a de novo design of  $\text{Au}_{36}(\text{SR})_{24}$  nanoclusters, from theoretical prediction to experimental synthesis and characterization of their physicochemical properties. The crystal structure of an  $\text{Au}_{36}(\text{SR})_{24}$  nanocluster perfectly matches the simulated structural pattern with  $\text{Au}_4$  tetrahedral units along a two-dimensional growth. The  $\text{Au}_{36}(\text{SR})_{24}$  nanocluster indeed differs from its structural isomer whose kernel is dissected in an  $\text{Au}_4$  tetrahedral manner along a one-dimensional growth. The structural isomerism in the  $\text{Au}_{36}(\text{SR})_{24}$  nanoclusters further induces distinct differences in ultrafast electron dynamics and chirality. This work will not only promote the atomically precise synthesis of nanoclusters enlightened by theoretical science, but also open up exciting opportunities for underpinning the widespread applications of structural isomers with atomic precision.

<sup>1</sup>School of Chemistry and Chemical Engineering, Nanjing University, 210093 Nanjing, China. <sup>2</sup>School of Physical Science and Technology, Ningbo University, 315211 Ningbo, China. <sup>3</sup>School of Physics, Nanjing University, 210093 Nanjing, China. <sup>4</sup>Zhangjiang Laboratory, Shanghai Advanced Research Institute, Chinese Academy of Sciences, 201210 Shanghai, China. <sup>5</sup>Tsinghua University-Peking University Joint Center for Life Sciences, School of Life Sciences, Tsinghua University, 100084 Beijing, China. <sup>6</sup>These authors contributed equally: Xu Liu, Wen Wu Xu, Xinyu Huang. ✉email: [cfzhang@nju.edu.cn](mailto:cfzhang@nju.edu.cn); [gaoyi@zjlab.org.cn](mailto:gaoyi@zjlab.org.cn); [zhuyan@nju.edu.cn](mailto:zhuyan@nju.edu.cn)

Thiolate-protected atomically precise gold nanoclusters referred to as  $\text{Au}_n(\text{SR})_m$  ( $n$  = gold atom number;  $m$  = ligand number) constitute a generation of gold nanoparticles and exhibit unique physical and chemical properties in optics, electronics, catalysis, chirality, and sensing<sup>1–9</sup>. Since the total structure of  $\text{Au}_{102}(\text{SR})_{44}$  was resolved<sup>10</sup>, the synthesis of one pot for one size starts to bloom and gold nanoclusters are constantly springing up<sup>11–18</sup>. However, despite the significant advances in  $\text{Au}_n(\text{SR})_m$  nanocluster studies, several critical issues remain still unclear, e.g. what exactly determines the structure of nanoclusters and what are real growth behaviors of nanoclusters in the solution phase? Moreover, whether the experimentalists can synthesize the specific nanoclusters based on the theoretical design is still challenging. In this work, we first identify the most potential candidate of  $\text{Au}_n(\text{SR})_m$  nanoclusters by the grand unified model (GUM) and density functional theory (DFT) calculations. Further we synthesize this nanocluster and prove its distinct property in optics and chirality. The work demonstrates the feasibility of rational synthesis of nanoclusters based on de novo design.

In correlating the conventional characterization information with the growth mechanism of nanoclusters, extensive studies have been applied to the combination of experimental and theoretical results to explore the growth of the basic structural units into smart structures<sup>19–28</sup>. Among these works,  $\text{Au}_4$  tetrahedron identified as a building block can be assembled into a series of  $\text{Au}_n(\text{SR})_m$  nanoclusters<sup>20,21,29–33</sup>. Especially, the solved crystal structures of a periodic series with a unified formula of  $\text{Au}_{8n+4}(\text{TBBT})_{4n+8}$  ( $\text{TBBT}$  = 4-tert-butylbenzenethiol,  $n$  = 3–6) nanoclusters reflect that their kernels are adopted in the connection mode of  $\text{Au}_4$  tetrahedron along one dimension<sup>32</sup>. It should be noted that  $\text{Au}_{28}(\text{CHT})_{20}$  (the isomer of  $\text{Au}_{28}(\text{TBBT})_{20}$  to some extent, cyclohexanethiol (CHT)) also contains the one-dimensional  $\text{Au}_{14}$  kernel made up of  $\text{Au}_4$  units. Recently, the discovery of structural isomerism in the  $\text{Au}_{52}(\text{SR})_{32}$  provided the first example that the kernel of  $\text{Au}_{52}(\text{SR})_{32}$  isomer can be arranged in a two-dimensional growth of  $\text{Au}_4$  tetrahedra<sup>33</sup>. A question naturally is whether the  $\text{Au}_4$  tetrahedron-based two-dimensional growth mode can be further extended to hitherto non-synthesized isomers in the family of  $\text{Au}_{8n+4}(\text{SR})_{4n+8}$ .

To address this, we initiate theoretical studies to predict the structures of a series of  $\text{Au}_{8n+4}(\text{SR})_{4n+8}$  with  $\text{Au}_4$  tetrahedron as the building unit in a two-dimensional growth pattern. Subsequently, we identify an  $\text{Au}_{36}(\text{SR})_{24}$  packed in two-dimensional mode that has the highest stability among all the isomers, which would be an ideal candidate for experimental synthesis to fill in one of missing isomers in the family. By calculation-assisted nanoclusters discovery, a couple of isomeric  $\text{Au}_{36}(\text{SR})_{24}$  nanoclusters protected by 3,5-dimethylbenzenethiol (DMBT) are successfully synthesized and their crystal structures accurately match the predicted ones. The  $\text{Au}_{36}(\text{DMBT})_{24}$  nanocluster packed in two-dimensional mode is chiral, whereas the other isomer whose structure is identical to the previously reported  $\text{Au}_{36}(\text{TBBT})_{24}$  is achiral. The two  $\text{Au}_{36}(\text{DMBT})_{24}$  nanoclusters also exhibit dramatic differences in ultrafast dynamics.

## Results

**Theoretical prediction.** Based on GUM, there is a potential two-dimensional growth pattern, in which the growth of gold kernels in thiolate-protected gold nanoclusters can be viewed as the sequent addition of elementary blocks (tetrahedral  $\text{Au}_4$  in this case) obeying duet rule<sup>21,28</sup>. As shown in Fig. 1, there are two types of face-centered cubic (fcc) growth pattern for the kernels of  $\text{Au}_{8n+4}(\text{SR})_{4n+8}$  ( $n$  = 3, 4, 5, 6) using  $\text{Au}_4$  building blocks. Starting from the predicted  $\text{Au}_{28}(\text{SR})_{20}$  (a3 in Fig. 1)<sup>22</sup>, two  $\text{Au}_4$

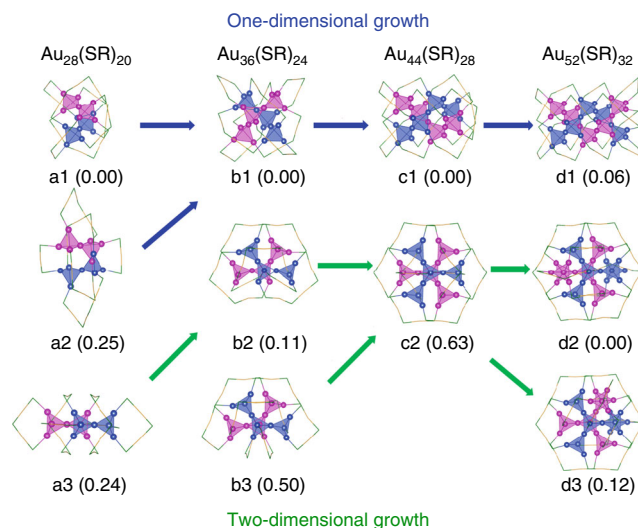


**Fig. 1** The growth patterns of  $\text{Au}_{8n+4}(\text{SR})_{4n+8}$  ( $n$  = 3–6) nanoclusters.

The values in brackets are the relative energies (eV). Note that structures of a1/b1/c1/d1 (TBBT as ligand) and a2 (CHT as ligand) are experimentally determined. The arrows in blue and green denote the one-dimensional and two-dimensional growth, respectively. According to the relative energies, b2 of  $\text{Au}_{36}(\text{SR})_{24}$  and d2 of  $\text{Au}_{52}(\text{SR})_{32}$  are the most potential candidates among the predicted isomers. Color labels: green = S, blue/magenta/yellow = Au. The C and H atoms are omitted for clarity.

units are fused with the  $\text{Au}_{14}$  kernel of  $\text{Au}_{28}(\text{SR})_{20}$  (a3 in Fig. 1) by sharing two gold atoms to form a new  $\text{Au}_{20}$  kernel, resulting in two  $\text{Au}_{36}(\text{SR})_{24}$  isomers (b2 and b3 in Fig. 1). Continuing fusing two  $\text{Au}_4$  units with the  $\text{Au}_{20}$  kernel of  $\text{Au}_{36}(\text{SR})_{24}$  can form an  $\text{Au}_{44}(\text{SR})_{28}$  isomer with  $\text{Au}_{26}$  kernel (c2 in Fig. 1). Following the same way, two different  $\text{Au}_{32}$  kernels can be obtained to form two  $\text{Au}_{52}(\text{SR})_{32}$  isomers (d2 and d3 in Fig. 1). Among them, the d2 of  $\text{Au}_{52}(\text{SR})_{32}$  protected by 2-phenylethanethiol (denoted as PET) was experimentally determined<sup>33</sup>. In this work, as illustrated in Fig. 1, totally four new isomers for  $\text{Au}_{8n+4}(\text{SR})_{4n+8}$  series have been theoretically predicted based on GUM. The series follow the two-dimensional growth mode (green arrows in Fig. 1), which is completely different from the one-dimensional double-helical growth for old series (blue arrows in Fig. 1).

All the predicted isomers (–R group is replaced by –H) were fully optimized using DFT method implemented in the Gaussian 09 program package<sup>34</sup>, including the TPSS functional<sup>35</sup> and the all-electron basis set 6–31 G\* for H and S, effective-core basis set LANL2DZ for Au. Among the predicted isomers shown in Fig. 1, the isomer b2 of  $\text{Au}_{36}(\text{SR})_{24}$  is only 0.11 eV higher in energy than b1, implying that this structure may be stable and accessible. In addition, this cluster has a large HOMO–LUMO (HOMO/LUMO: the highest/lowest occupied/unoccupied molecular orbital) gap and all positive harmonic vibrational frequencies (Supplementary Table 1), indicating its thermal and chemical stability. Thus, it motivates us to synthesize this most potential candidate based on the GUM-guided prediction.

**Synthesis and characterization.** The b1 and b2 isomers in  $\text{Au}_{36}(\text{SR})_{24}$  can be simultaneously synthesized using a two-step size-focusing method when DMBT was selected as the protected ligand. The two nanoclusters were denoted as  $\text{Au}_{36}(\text{DMBT})_{24}$ -1D and  $\text{Au}_{36}(\text{DMBT})_{24}$ -2D according to the growth modes (vide infra). Electrospray ionization mass spectra (ESI-MS) showed the  $m/z$  5192.02 peak with +2 charge for both nanoclusters (Supplementary Fig. 1), corresponding to  $[\text{Au}_{36}(\text{DMBT})_{24}\text{-}2\text{e}]^{2+}$  (calculation: 5192.09 Da; deviation: 0.07 Da). The observed

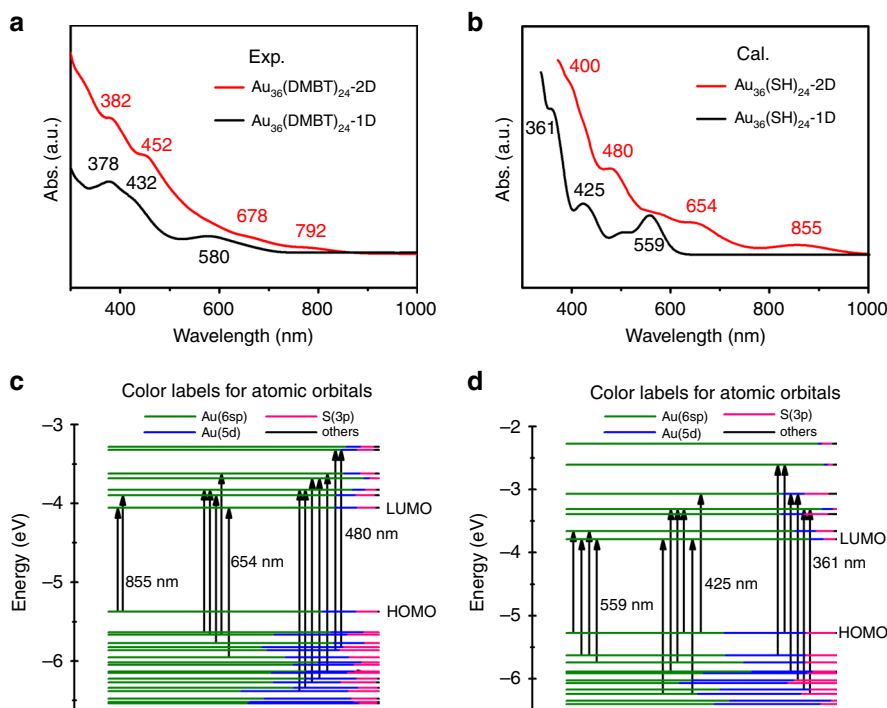


**Fig. 2** The optical absorption properties of  $\text{Au}_{36}(\text{DMBT})_{24}$  nanoclusters. **a** Experimental UV-vis spectra of  $\text{Au}_{36}(\text{DMBT})_{24-2\text{D}}$  and  $\text{Au}_{36}(\text{DMBT})_{24-1\text{D}}$ . **b** Calculated UV-vis spectra of  $\text{Au}_{36}(\text{SH})_{24-2\text{D}}$  and  $\text{Au}_{36}(\text{SH})_{24-1\text{D}}$ . The values in the black or red are the wavelength (nm) corresponding to the absorption peaks. Molecular orbital (MO) energy level diagrams for **c**  $\text{Au}_{36}(\text{SH})_{24-2\text{D}}$  and **d**  $\text{Au}_{36}(\text{SH})_{24-1\text{D}}$ . The energies are in eV. Various colors are used to mark relative contributions (line length with color labels) of different orbitals. The major orbital contributions from the Au(6sp), Au(5d), and S(3p) are in olive, blue, and pink, respectively. The values in the black are the wavelength (nm) corresponding to the absorption peaks.

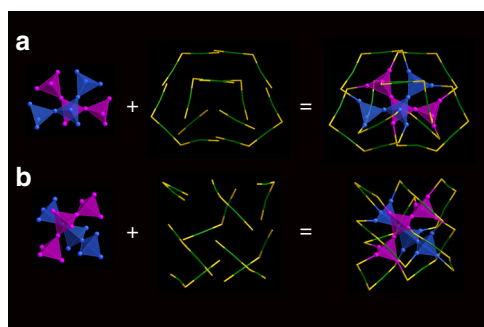


**Fig. 3** Crystal structures of the  $\text{Au}_{36}(\text{DMBT})_{24}$  nanoclusters. Structural frameworks of **a**  $\text{Au}_{36}(\text{DMBT})_{24-2\text{D}}$  and **b**  $\text{Au}_{36}(\text{DMBT})_{24-1\text{D}}$  shown in tetrahedral  $\text{Au}_4$  networks. Color labels: yellow = S, blue/magenta/green = Au. The C and H atoms are omitted for clarity.

isotopic distributions were in perfect agreement with the simulated ones, further verifying the accurate formula of  $\text{Au}_{36}(\text{DMBT})_{24}$  nanoclusters.

Figure 2a showed the optical absorption spectra of  $\text{Au}_{36}(\text{DMBT})_{24}$ .  $\text{Au}_{36}(\text{DMBT})_{24-2\text{D}}$  exhibited the two-step peaks at 382 and 452 nm and two broad peaks at 678 and 792 nm, respectively, while  $\text{Au}_{36}(\text{DMBT})_{24-1\text{D}}$  showed the two distinct peaks at 378 and 580 nm and one shoulder peak at 432 nm. The calculated UV-vis spectra of  $\text{Au}_{36}(\text{SH})_{24-2\text{D}}$  and  $\text{Au}_{36}(\text{SH})_{24-1\text{D}}$  were presented in Fig. 2b to reproduce the experimental results using linear response time-dependent density functional theory (TDDFT). The lowest 450 singlet-to-singlet excitation states were evaluated. As shown in Fig. 2b, the theoretical spectra can well reproduce the results of experimental measurements. Four absorption peaks (400, 480, 654, and 855 nm) for  $\text{Au}_{36}(\text{SH})_{24-2\text{D}}$  and three absorption peaks (361, 425, and 559 nm) for

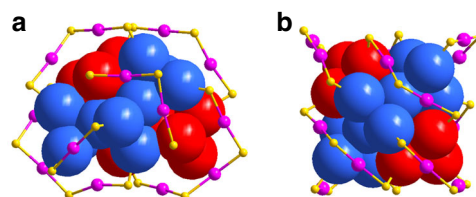


**Fig. 4** Comparison of the  $\text{Au}_{36}(\text{DMBT})_{24}$  structures. Structural frameworks of **a**  $\text{Au}_{36}(\text{DMBT})_{24-2\text{D}}$  and **b**  $\text{Au}_{36}(\text{DMBT})_{24-1\text{D}}$  shown in stacking mode. Color labels: yellow = S, blue/magenta/red = Au. The C and H atoms are omitted for clarity.

$\text{Au}_{36}(\text{SH})_{24-1\text{D}}$  can be observed. Further examination of the Kohn–Sham (KS) molecular orbital (MO) energy levels and atomic orbital components in each KS MO of  $\text{Au}_{36}(\text{SH})_{24-2\text{D}}$  and  $\text{Au}_{36}(\text{SH})_{24-1\text{D}}$  indicate that the absorption peaks mainly involve the  $\text{Au}(sp) \rightarrow \text{Au}(sp)$  transitions (Fig. 2c, d). Accordingly, the optical energy gaps were determined to be 1.36 eV for  $\text{Au}_{36}(\text{DMBT})_{24-2\text{D}}$  and 1.71 eV for  $\text{Au}_{36}(\text{DMBT})_{24-1\text{D}}$  based on the photon-energy scaled spectra (Supplementary Fig. 2), which were consistent with the corresponding calculated values of 1.31 and 1.74 eV (Supplementary Table 1).

Single-crystal X-ray crystallography studies showed that  $\text{Au}_{36}(\text{DMBT})_{24-2\text{D}}$  can be divided into a 20-atom gold kernel and eight external staple motifs (Figs. 3a and 4a). Twenty gold atoms in the kernel can be further viewed as two groups of  $\text{Au}_4$  tetrahedron which are arranged in a staggered mode, and this packing mode is in excellent agreement with the predicted two-dimensional growth (b2 in Fig. 1). The surface staple motifs can be divided into three categories: two monomeric  $\text{Au}_1(\text{SR})_2$ , two trimeric  $\text{Au}_3(\text{SR})_4$ , and four dimeric  $\text{Au}_2(\text{SR})_3$  (Figs. 3a and 4a). Note that both  $\text{Au}_3(\text{SR})_4$  and  $\text{Au}_2(\text{SR})_3$  staples are not in a plane

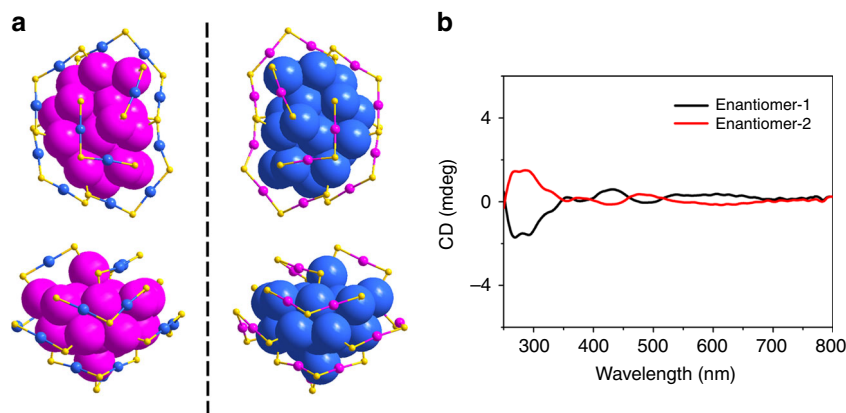


**Fig. 5** Chirality of the  $\text{Au}_{36}(\text{DMBT})_{24}\text{-2D}$  nanocluster. **a** The enantiomers of  $\text{Au}_{36}(\text{DMBT})_{24}\text{-2D}$  from top view (upper panel) and side view (lower panel). Color labels: yellow = S, blue/magenta = Au. The C and H atoms are omitted for clarity. **b** CD spectra of the separated enantiomers of  $\text{Au}_{36}(\text{DMBT})_{24}\text{-2D}$ .

(Supplementary Fig. 3). Alternatively, after cutting the gold atoms from  $\text{Au}_1(\text{SR})_2$  and  $\text{Au}_3(\text{SR})_4$  staples, the remaining 28 gold atoms can be constructed in a layer-by-layer fashion, which respectively consists of 6/8/8/6 atoms (Supplementary Fig. 4). This fashion is akin to a fcc structure of previously reported gold nanoclusters<sup>11,32,33</sup>.

As the counterpart of  $\text{Au}_{36}(\text{DMBT})_{24}\text{-2D}$ ,  $\text{Au}_{36}(\text{DMBT})_{24}\text{-1D}$  adopts a totally different configuration from  $\text{Au}_{36}(\text{DMBT})_{24}\text{-2D}$ , although it owns a 20-Au-atom kernel as well. In fact, the helical tetrahedron in the  $\text{Au}_{36}(\text{DMBT})_{24}\text{-1D}$  is along the one-dimensional growth (Figs. 3b and 4b), in contrast to  $\text{Au}_{36}(\text{DMBT})_{24}\text{-2D}$  (Figs. 3a and 4a), which are excellently consistent with the growing modes of the predicted b1 and b2 of  $\text{Au}_3(\text{SR})_{24}$  nanoclusters (Fig. 1). Notably, the  $\text{Au}_{36}(\text{SR})_{24}\text{-1D}$  and  $\text{Au}_{36}(\text{SR})_{24}\text{-2D}$  can be described by superatom network (SAN) model<sup>26</sup> with using the adaptive natural density partitioning (AdNDP) analysis<sup>36</sup> on the  $\text{Au}_{20}^{8+}$  of both  $\text{Au}_{36}(\text{SR})_{24}$ , which show the 12e valence electrons of  $\text{Au}_{36}(\text{SR})_{24}$  are equally distributed on six tetrahedral  $\text{Au}_4$  units, respectively (Supplementary Fig. 5). Thus, the  $\text{Au}_{20}$  core of each  $\text{Au}_{36}(\text{SR})_{24}$  can be viewed as a network of six 4c-2e (4c denotes 4 centers). Another notable issue is that the structural framework of  $\text{Au}_{36}(\text{DMBT})_{24}\text{-1D}$  is identical to that of reported  $\text{Au}_{36}(\text{TBBT})_{24}$ <sup>11</sup>. There are four non-planar and four co-planar staple motifs  $\text{Au}_2(\text{SR})_3$  in  $\text{Au}_{36}(\text{DMBT})_{24}\text{-1D}$  (Supplementary Fig. 3). After cutting the Au atoms from co-planar  $\text{Au}_2(\text{SR})_3$  staples, the remaining 28 Au atoms of  $\text{Au}_{36}(\text{DMBT})_{24}\text{-1D}$  are packed in a fcc structure (Supplementary Figs. 6 and 7). As we know, the previous studies showed the non-fcc vs. non-fcc isomerization appeared in the  $\text{Au}_{38}(\text{PET})_{24}$  isomers and the fcc vs. non-fcc isomerization existed in the  $\text{Au}_{42}(\text{TBBT})_{26}$  isomers<sup>15,37</sup>. Here the fcc vs. fcc isomerization is for the first time observed in the  $\text{Au}_{36}(\text{DMBT})_{24}$  isomers. In addition,  $\text{Au}_{36}(\text{DMBT})_{24}\text{-2D}$  can be irreversibly converted to  $\text{Au}_{36}(\text{DMBT})_{24}\text{-1D}$  at 333 K for 2 h, which indicates that the latter is more stable than the former.

To further corroborate the mechanism of two-dimensional growth in the series of  $\text{Au}_{8n+4}(\text{SR})_{4n+8}$  nanoclusters, we tried to synthesize c2 isomer of  $\text{Au}_{44}(\text{SR})_{28}$  using various synthetic methods, e.g., one-pot reduction, size-focusing, and thermal conversion (the synthesis details are shown in Methods section). Different ligands were employed such as 3-methylbenzenethiol, 4-isopropylbenzenethiol, 2,4-dimethylbenzenethiol, etc. The experimental conditions were controlled by tuning temperature and pH in different solvents. Under the above attempts, we obtained  $\text{Au}_{36}(\text{SR})_{24}\text{-1D}$ ,  $\text{Au}_{44}(\text{SR})_{28}\text{-1D}$ , and other unknown nanoclusters, which were indicated by UV-vis (Supplementary Fig. 8) and ESI-MS spectra (Supplementary Figs. 9 and 10). The c2 isomer of  $\text{Au}_{44}(\text{SR})_{28}$  (denoted as  $\text{Au}_{44}(\text{SR})_{28}\text{-2D}$ ) was not

obtained, which is possibly because the  $\text{Au}_{44}(\text{SR})_{28}\text{-2D}$  (0.63 eV) is notably higher in energy than  $\text{Au}_{44}(\text{SR})_{28}\text{-1D}$  (0 eV) (Fig. 1). In addition, as is known, the synthesis of nanoclusters involves kinetic control in the early stage and the carbon tail of the thiol ligands often plays an important role. While we believe the  $\text{Au}_{44}(\text{SR})_{28}\text{-2D}$  would be attainable, their syntheses might take an exhaustive search for the right HS-R to reach the exact conditions. Therefore, we have to leave this to future work. Notably, the d2 isomer of  $\text{Au}_{52}(\text{SR})_{32}$  can be synthesized with the assistance of acid<sup>33</sup>. The  $\text{Au}_{32}$  kernel of  $\text{Au}_{52}(\text{TBBT})_{32}$  (d1 isomer) adopts the one-dimensional growth of the  $\text{Au}_4$  units (Supplementary Fig. 11a)<sup>32</sup>, while the kernel of  $\text{Au}_{52}(\text{PET})_{32}$  (d2 isomer) consists of 32 gold atoms that are arranged along two-dimensional direction based on the  $\text{Au}_4$  tetrahedron (Supplementary Fig. 11b). Thus, the  $\text{Au}_{52}(\text{PET})_{32}$  nanocluster further supports the possibility of the two-dimensional growth for  $\text{Au}_4$  units of  $\text{Au}_{8n+4}(\text{SR})_{4n+8}$  proposed in this work.

**Chirality.**  $\text{Au}_{36}(\text{DMBT})_{24}\text{-2D}$  is chiral, as the  $\text{Au}_{20}$  kernel and surface staple units are both arranged in a chiral pattern (Fig. 5a), while  $\text{Au}_{36}(\text{DMBT})_{24}\text{-1D}$  is achiral due to no mirror plane occurring in the metal kernel and the surface staples (Figs. 3b and 4b). We separated the  $\text{Au}_{36}(\text{DMBT})_{24}\text{-2D}$  enantiomers by high-performance liquid chromatography (HPLC) (Supplementary Fig. 12) and studied its chirality by circular dichroism (CD)<sup>38–42</sup>. As shown in Fig. 5b, the pair of  $\text{Au}_{36}(\text{DMBT})_{24}\text{-2D}$  enantiomers showed a mirror symmetry for multiple peaks in the CD spectra, which were respectively centered at 268, 292, 329, 355, 380, 430, 487, and 615 nm in the UV-vis spectral region. The theoretically simulated CD spectra for  $\text{Au}_{36}(\text{SH})_{24}$  enantiomers agreed with the experimental spectra (Supplementary Fig. 13).

**Ultrafast electron dynamics.** The dynamics of excited states in the two  $\text{Au}_{36}(\text{DMBT})_{24}$  nanoclusters were studied by using transient absorption (TA) spectroscopic measurements. Figure 6a, b compared the femtosecond-resolved TA data of two isomers pumped at 400 nm. We carried out the global fitting analysis to extract the evolution associated spectra (EAS) of the isomers, as shown in Fig. 6c, d. Except for some slight wavelength shifted, the spectral characteristics showed similar features for both nanoclusters with excited-state absorption near 500 nm and ground-state bleach near 600 nm, respectively. Nonetheless, the temporal dynamics exhibited remarkable differences for the two isomers. For the  $\text{Au}_{36}(\text{DMBT})_{24}\text{-1D}$  nanocluster, the experimental data can be reproduced by three processes with lifetime parameters of 0.5 ps, 7 ps, and >1 ns (Fig. 6d), respectively. In

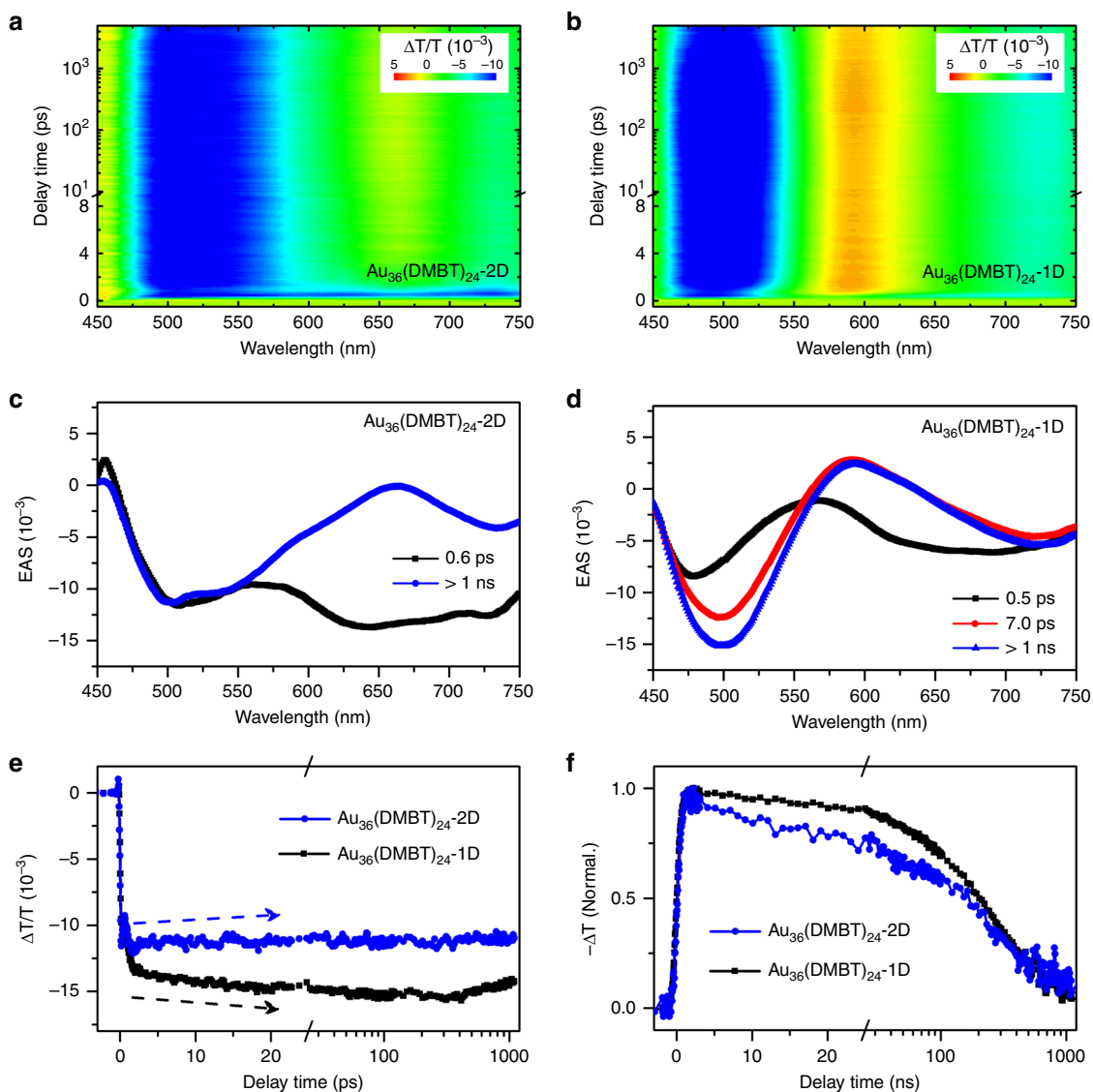


**Fig. 6** Excited-state dynamics of  $\text{Au}_{36}(\text{DMBT})_{24}$  nanoclusters. Femtosecond-resolved transient absorption data recorded from **a**  $\text{Au}_{36}(\text{DMBT})_{24-2\text{D}}$  and **b**  $\text{Au}_{36}(\text{DMBT})_{24-1\text{D}}$ . Spectral features of different delay components derived from global fitting analysis for **c**  $\text{Au}_{36}(\text{DMBT})_{24-2\text{D}}$  and **d**  $\text{Au}_{36}(\text{DMBT})_{24-1\text{D}}$ . **e** Femtosecond-resolved and **f** nanosecond-resolved dynamic traces of the two nanoclusters.

analogy to the previously reported results on  $\text{Au}_{36}(\text{TBBT})_{24}$  nanocluster, the three components can be attributed to ultrafast  $S_n \rightarrow S_1$  internal conversion, structural relaxation, and carrier recombination, respectively<sup>43</sup>. However, the component of structural relaxation ( $\sim 7$  ps) was not present in the data recorded from the  $\text{Au}_{36}(\text{DMBT})_{24-2\text{D}}$  nanocluster (Fig. 6c). Such a difference was explicitly manifested in the dynamics probed at 500 nm (Fig. 6e; more meticulous comparison shown in Supplementary Fig. 14), where a delayed rise in the excited-state absorption signal observed from the  $\text{Au}_{36}(\text{DMBT})_{24-1\text{D}}$  sample was absent in the data recorded from the  $\text{Au}_{36}(\text{DMBT})_{24-2\text{D}}$  sample. This marked difference between the electron dynamics in the two isomers is probably related to their different structures: the picosecond component with lifetime of  $\sim 7$  ps in  $\text{Au}_{36}(\text{DMBT})_{24-1\text{D}}$  nanoclusters is the structural relaxation due to the expansion or torsion of one-dimensional chains after excitation<sup>43</sup>, while the  $\sim 7$  ps component is not observed in  $\text{Au}_{36}(\text{DMBT})_{24-2\text{D}}$  nanoclusters, which may be due to the limitation of the conformation changes in the two-dimensional kernel. In addition, it was found that the carrier recombination in

the  $\text{Au}_{36}(\text{DMBT})_{24-2\text{D}}$  sample became slightly faster than that in the  $\text{Au}_{36}(\text{DMBT})_{24-1\text{D}}$  sample (Fig. 6f). These observations are interesting that  $\text{Au}_{36}(\text{DMBT})_{24-2\text{D}}$  and  $\text{Au}_{36}(\text{DMBT})_{24-1\text{D}}$  have same chemical compositions, but show drastic differences in their optical features and electron dynamics.

## Discussion

On the basis of the theoretical prediction for decision making, we have successfully synthesized a pair of isomeric  $\text{Au}_{36}(\text{DMBT})_{24}$  nanoclusters by selecting an appropriate ligand: one is constructed from  $\text{Au}_4$  tetrahedral units along the two-dimensional growth, whereas the other is patterned in an  $\text{Au}_4$  tetrahedral manner along the one-dimensional growth. The isomerism in the two  $\text{Au}_{36}(\text{DMBT})_{24}$  nanoclusters indeed induces evident differences in physicochemical properties, such as optics, chirality, and ultrafast dynamics. This de novo design of  $\text{Au}_{36}(\text{SR})_{24}$  is expected to stimulate further work on the synthetic chemistry guided by theoretical studies as well as on the practical applications of atomically precise isomeric nanoclusters.

## Methods

**Materials.** All chemicals and reagents are commercially available and used without further purification. 3,5-dimethylbenzenethiol (3,5-DMBT, 98.0%), 4-tert-butylbenzenethiol (TBBT, 98.0%), 4-methylbenzenethiol (4-MBT, 98.0%), 3-methylbenzenethiol (3-MBT, 97.0%), 4-ethylbenzenethiol (4-EBT, 97.0%), 4-isopropylbenzenethiol (4-IPBT, 96.0%), 2,4-dimethylbenzenethiol (2,4-DMBT, 95.0%), 2-phenylethanethiol (PET, 97.0%), 4-tert-butyl benzyl mercaptan (97.0%), benzyl mercaptan (98.0%), and tetra-octylammonium bromide (TOAB, 98.0%) were purchased from Aladdin. Tetrachloroauric (III) acid ( $\text{HAuCl}_4 \cdot 4\text{H}_2\text{O}$ , 99.9%), sodium borohydride ( $\text{NaBH}_4$ , 98.0%), methanol ( $\text{CH}_3\text{OH}$ , 99.5%), dichloromethane ( $\text{CH}_2\text{Cl}_2$ , 99.0%), acetonitrile ( $\text{CH}_3\text{CN}$ , 99.0%), toluene ( $\text{PhCH}_3$ , 99.5%), and petroleum ether (AR) were obtained from Sinopharm Chemical Reagent Co. Ltd. The water used in all experiments was ultrapure with the resistivity of 18.2  $\text{M}\Omega\text{-cm}$  produced by a Milli-Q NANO pure water system.

**Synthesis of  $\text{Au}_{36}(\text{DMBT})_{24}$  nanoclusters.**  $\text{Au}_{36}(\text{DMBT})_{24}\text{-2D}$  and  $\text{Au}_{36}(\text{DMBT})_{24}\text{-1D}$  nanoclusters were simultaneously synthesized using a two-step size-focusing method. Step 1: 50 mg of  $\text{HAuCl}_4 \cdot 4\text{H}_2\text{O}$  (0.12 mmol) dissolved in 1 mL water was mixed with 10 mL  $\text{CH}_2\text{Cl}_2$  containing TOAB (80 mg, 0.15 mmol). After vigorously stirring for 20 min, the organic layer was transferred into a 50-mL flask and 60- $\mu\text{L}$  3,5-dimethylbenzenethiol (DMBT) was injected. The above mixture was stirred until the color of the solution was clear, then an aqueous solution containing 25 mg of  $\text{NaBH}_4$  was added at once. The reduction was allowed to proceed for 6 h. After that, the reaction mixture was dried by a rotary evaporator, and the obtained precipitates were washed with methanol three times to remove excess ligands and salts. Step 2: the obtained precursor was extracted with 0.5 mL toluene and then etched by 0.5 mL DMBT for 48 h at room temperature. The crude product was washed with  $\text{CH}_3\text{OH}$  and separated by thin-layer chromatography. Both  $\text{Au}_{36}(\text{DMBT})_{24}\text{-2D}$  and  $\text{Au}_{36}(\text{DMBT})_{24}\text{-1D}$  nanoclusters were crystallized in toluene/acetonitrile solution by vapor diffusion over two weeks.

**Synthetic attempts for  $\text{Au}_{44}(\text{SR})_{28}\text{-2D}$  nanoclusters.** (1) Size-focusing method: the nanoclusters were prepared from the ligand (4-methylbenzenethiol, 3-methylbenzenethiol, 4-ethylbenzenethiol, 4-isopropylbenzenethiol, or 4-tert-butylphenylthiol) in place of DMBT under otherwise identical experimental conditions of  $\text{Au}_{36}(\text{DMBT})_{24}$  mentioned above. (2) One-pot reduction method: 50 mg of  $\text{HAuCl}_4 \cdot 4\text{H}_2\text{O}$  (0.12 mmol) and 100 mg of TOAB were dissolved in 17 mL solvent such as tetrahydrofuran, dichloromethane, or ethyl acetate. After vigorously stirring for 20 min, 190  $\mu\text{L}$  organic ligand (e.g., benzyl mercaptan, 3,5-dimethylbenzenethiol, 2,4-dimethylbenzenethiol, 4-tert-butyl benzyl mercaptan, or 2-phenylethanethiol) was injected. The above mixture was stirred until the color of the solution was clear (~2 h), and then the pH was adjusted by adding  $\text{H}^+$  or  $\text{OH}^-$  prior to reduction. An aqueous solution containing 60 mg of  $\text{NaBH}_4$  was added in the above mixture at once and the reduction was allowed to proceed for ~14 h. After that, the solution was evaporated and the residue was washed with  $\text{CH}_3\text{OH}$  for three times. Finally, the product was separated by thin-layer chromatography. (3) Thermal conversion method: e.g., 20 mg of  $\text{Au}_{44}(\text{DMBT})_{28}\text{-1D}$  was dissolved in 2 mL toluene and 2 mL 2,4-dimethylbenzenethiol. The mixture was maintained at 60  $^\circ\text{C}$  for 24 h. The crude product was washed with  $\text{CH}_3\text{OH}$  and separated by thin-layer chromatography.

**X-ray crystallography.** The single-crystal X-ray diffraction data for  $\text{Au}_{36}(\text{DMBT})_{24}\text{-2D}$  and  $\text{Au}_{36}(\text{DMBT})_{24}\text{-1D}$  nanoclusters were collected on a Bruker D8 VENTURE using Mo K $\alpha$  radiation ( $\lambda = 0.71073 \text{ \AA}$ ) and Ga K $\alpha$  radiation ( $\lambda = 1.34139 \text{ \AA}$ ), respectively. The structure was solved by ShelxT and refined by ShelXL. Platon-Squeeze program was used to remove the contributions of disordered solvent.

**Chirality measurements.** The enantiomers of  $\text{Au}_{36}(\text{DMBT})_{24}\text{-2D}$  were separated by HPLC on a DIONEX UltiMate 3000 system (Thermo SCIENTIFIC) equipped with Chiral AS column (DAICEL), where the mobile phase was isopropanol/hexane = 2/98, the flow rate was set at 0.5 mL  $\text{min}^{-1}$  and the eluents were collected at different times. CD spectra were carried out on CD JASCO J-810 and the enantiomers were dissolved in dichloromethane for CD measurements.

**Ultrafast optical measurements.** A Ti:sapphire regenerative amplifier (Libra, Coherent Inc.) was used for TA spectroscopy. For femtosecond TA experiment, the optical delay between the pump and probe beams was enabled by a translation stage. The pump beam at 400 nm wavelength was from the second harmonic generation of BBO crystal pumped by a portion of laser from the regenerative amplifier. The probe beam was a broadband supercontinuum light source generated by focusing a small portion of the femtosecond laser beam onto a 3-mm-thick sapphire plate. The time resolution in our fs experiments was ~150 fs. The TA signal is then analyzed by a silicon charge-coupled device (CCD; S11071-1104, Hamamatsu) with a monochromator (Acton 2358, Princeton Instrument) at 1 kHz enabled by a custom-built control board from Entwicklungsbuero Stresing. The signal-to-noise ratio in differential transmission was better than  $5 \times 10^{-5}$  after accumulating and averaging 1000 pump-on and pump-off shots for each data point. The angle between the polarized pump and probe beams was set at the magic angle. For nanosecond TA spectroscopy, we used a sub-nanosecond laser (Picolo AOT MOPA, InnoLas) at

355 nm (pulse duration ~0.8 ns) to excite the samples. The laser was synchronized to the probe pulse with a desired delay by an electronic delay generator (SRS DG645, Stanford Research System). The diameters of the pump beam spots in fs and ns experiments were ~1 mm and 0.3 mm, respectively. The diameter of probe beam was ~0.2 mm. The pump fluence was kept ~100  $\mu\text{J cm}^{-2}$  in both experiments. The clusters dissolved in toluene were placed in 1 mm path length cuvettes for TA measurements. The optical density of samples at 550 nm was ~0.3.

## Data availability

The X-ray crystallographic coordinates for structures reported in this study have been deposited at the Cambridge Crystallographic Data Centre (CCDC), under deposition numbers CCDC 1922740 and CCDC 1922741. These data can be obtained free of charge from The Cambridge Crystallographic Data Centre via [www.ccdc.cam.ac.uk/data\\_request/cif](http://www.ccdc.cam.ac.uk/data_request/cif).

Received: 18 September 2019; Accepted: 9 June 2020;

Published online: 03 July 2020

## References

- Higaki, T. et al. Atomically tailored gold nanoclusters for catalytic applications. *Angew. Chem. Int. Ed.* **58**, 8291–8302 (2019).
- Kang, X. & Zhu, M. Tailoring the photoluminescence of atomically precise nanoclusters. *Chem. Soc. Rev.* **48**, 2422–2457 (2019).
- Chakraborty, I. & Pradeep, T. Atomically precise clusters of noble metals: emerging link between atoms and nanoparticles. *Chem. Rev.* **117**, 8208–8271 (2017).
- Zhu, Y. et al. Enantioseparation of  $\text{Au}_{20}(\text{PP}_3)_4\text{Cl}_4$  clusters with intrinsically chiral cores. *Angew. Chem. Int. Ed.* **57**, 9059–9063 (2018).
- Luo, Z. et al. From aggregation-induced emission of Au(I)-thiolate complexes to ultrabright Au(0)@Au(I)-thiolate core-shell nanoclusters. *J. Am. Chem. Soc.* **134**, 16662–16670 (2012).
- Turner, M. et al. Selective oxidation with dioxygen by gold nanoparticle catalysts derived from 55-atom clusters. *Nature* **454**, 981–984 (2008).
- Liu, Y. et al. Central doping of a foreign atom into the silver cluster for catalytic conversion of  $\text{CO}_2$  toward C-C bond formation. *Angew. Chem. Int. Ed.* **57**, 9775–9779 (2018).
- Narouz, M. R. et al. N-heterocyclic carbene-functionalized magic-number gold nanoclusters. *Nat. Chem.* **11**, 419–425 (2019).
- Shi, L. et al. Self-assembly of chiral gold clusters into crystalline nanocubes of exceptional optical activity. *Angew. Chem. Int. Ed.* **56**, 15397–15401 (2017).
- Jadzinsky, P. D., Calero, G., Ackerson, C. J., Bushnell, D. A. & Kornberg, R. D. Structure of a thiol monolayer-protected gold nanoparticle at 1.1 Å resolution. *Science* **318**, 430–433 (2007).
- Zeng, C. et al. Total structure and electronic properties of the gold nanocrystal  $\text{Au}_{36}(\text{SR})_{24}$ . *Angew. Chem. Int. Ed.* **51**, 13114–13118 (2012).
- Zeng, C., Chen, Y., Kirschbaum, K., Lambright, K. J. & Jin, R. Emergence of hierarchical structural complexities in nanoparticles and their assembly. *Science* **354**, 1580–1585 (2016).
- Zhang, S. et al. Diphosphine-protected ultrasmall gold nanoclusters: opened icosahedral  $\text{Au}_{13}$  and hearted-shaped  $\text{Au}_8$  clusters. *Chem. Sci.* **9**, 1251–1258 (2018).
- Shen, H. et al. Highly robust but surface-active: N-heterocyclic carbene-stabilized  $\text{Au}_{25}$  nanocluster. *Angew. Chem. Int. Ed.* **58**, 17731–17735 (2019).
- Tian, S. et al. Structural isomerism in gold nanoparticles revealed by X-ray crystallography. *Nat. Commun.* **6**, 8667 (2015).
- Yang, S. et al. A new crystal structure of  $\text{Au}_{36}$  with a  $\text{Au}_{14}$  kernel co-capped by thiolate and chloride. *J. Am. Chem. Soc.* **137**, 10033–10035 (2015).
- Lei, Z., Li, J., Wan, X., Zhang, W. & Wang, Q. Isolation and total structure determination of an all-alkynyl-protected gold nanocluster  $\text{Au}_{144}$ . *Angew. Chem. Int. Ed.* **57**, 8639–8643 (2018).
- Takano, S., Hirai, H., Muramatsu, S. & Tsukuda, T. Hydride-doped gold superatom ( $\text{Au}_9\text{H}$ ) $^{2+}$ : synthesis, structure, and transformation. *J. Am. Chem. Soc.* **140**, 8380–8383 (2018).
- Pei, Y. & Zeng, X. Investigating the structural evolution of thiolate protected gold clusters from first-principles. *Nanoscale* **4**, 4054–4072 (2012).
- Liu, C., Pei, Y., Sun, H. & Ma, J. The nucleation and growth mechanism of thiolate-protected Au nanoclusters. *J. Am. Chem. Soc.* **137**, 15809–15816 (2015).
- Xu, W., Zhu, B., Zeng, X. & Gao, Y. A grand unified model for liganded gold clusters. *Nat. Commun.* **7**, 13574 (2016).
- Xu, W., Zeng, X. & Gao, Y. The structural isomerism in gold nanoclusters. *Nanoscale* **10**, 9476–9483 (2018).
- Natarajan, G., Mathew, A., Negishi, Y., Whetten, R. L. & Pradeep, T. A unified framework for understanding the structure and modifications of atomically

- precise monolayer protected gold clusters. *J. Phys. Chem. C* **119**, 27768–27785 (2015).
24. Aikens, C. M. Electronic and geometric structure, optical properties, and excited state behavior in atomically precise thiolate-stabilized noble metal nanoclusters. *Acc. Chem. Res.* **51**, 3065–3073 (2018).
25. Jiang, D., Overbury, S. H. & Dai, S. Structure of Au<sub>15</sub>(SR)<sub>13</sub> and its implication for the origin of the nucleus in thiolated gold nanoclusters. *J. Am. Chem. Soc.* **135**, 8786–8789 (2013).
26. Cheng, L., Yuan, Y., Zhang, X. & Yang, J. Superatom networks in thiolate-protected gold nanoparticles. *Angew. Chem. Int. Ed.* **52**, 9035–9039 (2013).
27. Walter, M. et al. A unified view of ligand-protected gold clusters as superatom complexes. *Proc. Natl Acad. Sci. USA* **105**, 9157–9162 (2008).
28. Xu, W., Zeng, X. & Gao, Y. Application of electronic counting rules for ligand-protected gold nanoclusters. *Acc. Chem. Res.* **51**, 2739–2747 (2018).
29. Gan, Z. et al. Fluorescent gold nanoclusters with interlocked staples and a fully thiolate-bound kernel. *Angew. Chem. Int. Ed.* **55**, 11567–11571 (2016).
30. Zeng, C. et al. Gold tetrahedra coil up: Kekule-like and double helical superstructures. *Sci. Adv.* **1**, e1500425 (2015).
31. Chen, Y. et al. Isomerism in Au<sub>28</sub>(SR)<sub>20</sub> nanocluster and stable structures. *J. Am. Chem. Soc.* **138**, 1482–1485 (2016).
32. Zeng, C. et al. Gold quantum boxes: on the periodicities and the quantum confinement in the Au<sub>28</sub>, Au<sub>36</sub>, Au<sub>44</sub>, and Au<sub>52</sub> magic series. *J. Am. Chem. Soc.* **138**, 3950–3953 (2016).
33. Zhuang, S. et al. The fcc structure isomerization in gold nanoclusters. *Nanoscale* **9**, 14809–14813 (2017).
34. Frisch, M. J. et al. *Gaussian 09*. (Gaussian, Inc., Wallingford CT, 2009).
35. Tao, J., Perdew, J. P., Staroverov, V. N. & Scuseria, G. E. Climbing the density functional ladder: nonempirical meta-generalized gradient approximation designed for molecules and solids. *Phys. Rev. Lett.* **91**, 146401 (2003).
36. Zubarev, D. Y. & Boldyrev, A. I. Developing paradigms of chemical bonding: adaptive natural density partitioning. *Phys. Chem. Chem. Phys.* **10**, 5207–5217 (2008).
37. Zhuang, S. et al. Fcc versus non-fcc structural isomerism of gold nanoparticles with kernel atom packing dependent photoluminescence. *Angew. Chem. Int. Ed.* **58**, 4510–4514 (2019).
38. Knoppe, S., Azoulay, R., Dass, A. & Bürgi, T. In situ reaction monitoring reveals a diastereoselective ligand exchange reaction between the intrinsically chiral Au<sub>38</sub>(SR)<sub>24</sub> and chiral thiols. *J. Am. Chem. Soc.* **134**, 20302–20305 (2012).
39. Knoppe, S., Dolamic, I., Dass, A. & Bürgi, T. Separation of enantiomers and CD spectra of Au<sub>40</sub>(SCH<sub>2</sub>CH<sub>2</sub>Ph)<sub>24</sub>: spectroscopic evidence for intrinsic chirality. *Angew. Chem. Int. Ed.* **51**, 7589–7591 (2012).
40. Dolamic, I., Knoppe, S., Dass, A. & Bürgi, T. First enantioseparation and circular dichroism spectra of Au<sub>38</sub> clusters protected by achiral ligands. *Nat. Commun.* **3**, 798 (2012).
41. Knoppe, S. & Bürgi, T. Chirality in thiolate-protected gold clusters. *Acc. Chem. Res.* **47**, 1318–1326 (2014).
42. He, X., Wang, Y., Jiang, H. & Zhao, L. Structurally well-defined sigmoidal gold clusters: probing the correlation between metal atom arrangement and chiroptical response. *J. Am. Chem. Soc.* **138**, 5634–5643 (2016).
43. Zhou, M. et al. Evolution of excited-state dynamics in periodic Au<sub>28</sub>, Au<sub>36</sub>, Au<sub>44</sub>, and Au<sub>52</sub> nanoclusters. *J. Phys. Chem. Lett.* **8**, 4023–4030 (2017).

## Acknowledgements

We thank the financial supports from National Natural Science Foundation of China (21773109, 91845104, and 21773287) and China Postdoctoral Science Foundation (2019M650106). We thank Shun Xu and Haoqi Liu for the preparation of nanoclusters.

## Author contributions

Ya.Z. conceived the project. X.L. synthesized the nanoclusters and grew the crystals. W.W.X., E.W., and Y.G. conducted the calculations. X.H., C.Z., and M.X. carried out ultrafast optical measurements. X.C. analyzed the enantiomers. Yu.Z. analyzed the crystal data. J.L. conducted the ESI-MS measurements. W.D. discussed the results. All authors wrote the manuscript.

## Competing interests

The authors declare no competing interests.

## Additional information

Supplementary information is available for this paper at <https://doi.org/10.1038/s41467-020-17132-5>.

Correspondence and requests for materials should be addressed to C.Z., Y.G. or Y.Z.

Peer review information *Nature Communications* thanks Longjiu Cheng and the other, anonymous, reviewer(s) for their contribution to the peer review of this work.

Reprints and permission information is available at <http://www.nature.com/reprints>

Publisher's note Springer Nature remains neutral with regard to jurisdictional claims in published maps and institutional affiliations.



**Open Access** This article is licensed under a Creative Commons Attribution 4.0 International License, which permits use, sharing, adaptation, distribution and reproduction in any medium or format, as long as you give appropriate credit to the original author(s) and the source, provide a link to the Creative Commons license, and indicate if changes were made. The images or other third party material in this article are included in the article's Creative Commons license, unless indicated otherwise in a credit line to the material. If material is not included in the article's Creative Commons license and your intended use is not permitted by statutory regulation or exceeds the permitted use, you will need to obtain permission directly from the copyright holder. To view a copy of this license, visit <http://creativecommons.org/licenses/by/4.0/>.

© The Author(s) 2020